



**HAL**  
open science

## Locating hydrothermal acoustic sources at Old Faithful Geyser using Matched Field Processing

Estelle Cros, Philippe Roux, Jean Vandemeulebrouck, S. Kedar

► **To cite this version:**

Estelle Cros, Philippe Roux, Jean Vandemeulebrouck, S. Kedar. Locating hydrothermal acoustic sources at Old Faithful Geyser using Matched Field Processing. *Geophysical Journal International*, 2011, 187 (1), pp.385-393. 10.1111/J.1365-246X.2011.05147.X . hal-00624592

**HAL Id: hal-00624592**

**<https://hal.science/hal-00624592>**

Submitted on 19 Sep 2011

**HAL** is a multi-disciplinary open access archive for the deposit and dissemination of scientific research documents, whether they are published or not. The documents may come from teaching and research institutions in France or abroad, or from public or private research centers.

L'archive ouverte pluridisciplinaire **HAL**, est destinée au dépôt et à la diffusion de documents scientifiques de niveau recherche, publiés ou non, émanant des établissements d'enseignement et de recherche français ou étrangers, des laboratoires publics ou privés.

# Locating hydrothermal acoustic sources at Old Faithful Geyser using Matched-Field Processing

E. Cros<sup>1</sup>, P. Roux<sup>2</sup>, J. Vandemeulebrouck<sup>1</sup>  
and S. Kedar<sup>3</sup>

<sup>1</sup> ISTerre, CNRS UMR5275, Université de Savoie, Campus Scientifique,  
73376 Le Bourget-du-Lac Cedex, France

<sup>2</sup> ISTerre, CNRS UMR5275, Université Joseph Fourier,  
Maison des Géosciences, BP 53,  
38041 Grenoble Cedex 9, France

<sup>3</sup> Jet Propulsion Laboratory, California Institute of Technology,  
Pasadena, CA 91109, USA

## 1 Summary

In 1992, a large and dense array of geophones was placed around the geyser vent of Old Faithful, in the Yellowstone National Park, in order to determine the origin of the seismic hydrothermal noise recorded at the surface of the geyser and to understand its dynamics. Old Faithful Geyser (OFG) is a small-scale hydrothermal system where a two-phase flow mixture erupts every 40 to 100 minutes in a high continuous vertical jet. Using Matched Field Processing (MFP) techniques on 10-min-long signal, we localize the source of the seismic pulses recorded at the surface of the geyser. Several MFP approaches are compared in this study, the frequency-incoherent and frequency coherent approach, as well as the linear Bartlett processing and the non-linear Minimum Variance Distorsionless Response (MVDR) processing. The different MFP techniques used give the same source position with better focalization in the case of the MVDR processing. The retrieved source position corresponds to the geyser conduit at a depth of 12 m and the localization is in good agreement with in-situ measurements made at Old Faithful in past studies.

Keywords: Hydrothermal systems ; Volcano seismology ; Wave propagation ; North America

## 2 Introduction

1 Old Faithful Geyser (OFG) is located in the Upper Geyser Basin (UGB) in the Yellowstone  
2 National Park. The basin is approximately  $3.2 \times 0.8$  km and is on the periphery of the  
3 Mallard Lake resurgent dome within the Yellowstone Caldera. The caldera was formed  
4 640,000 years ago by a giant eruption and measures  $80 \times 50$  km. The presence of a  
5

6 complex magmatic reservoir system beneath the caldera (Fournier, 1989; Husen et al.,  
7 2004; Miller & Smith, 1999) delivers the heat that maintain the hot springs, geysers and  
8 mud pots on the different basins. The heat flux density calculated with a river chloride  
9 inventory method is estimated at  $2000 \text{ mW m}^{-2}$  over the  $2900 \text{ km}^2$  corresponding to the  
10 caldera area (Fournier, 1989). The Yellowstone thermal water is mainly meteoric in origin  
11 with magmatic contribution less than a few percent (Fournier, 1989).

12 The edifice of OFG is essentially conical with a diameter of 60 m, and is characterized  
13 by a 4 m high geyserite vent concretion, with an opening of  $2 \text{ m} \times 1 \text{ m}$ , and an irregular,  
14 elongated fissure-like conduit (Hutchinson et al., 1997). It is one of the most studied  
15 geyser in the world because of its regularity and the short interval between two eruptions  
16 which makes its study very convenient. The time interval between two eruptions follows  
17 a bimodal distribution, between 40 and 100 minutes, with a principal mode centered on  
18 80 minutes. The eruption is characterized by a continuous vertical jet of water and steam  
19 at a height of 30 to 50 m lasting for 1 to 6 min for a total discharge of water between 14  
20 000 and 32 000 l.

21 Most of the studies on Old Faithful focalize on the evolution of the time interval  
22 between two eruptions (Hurwitz et al., 2008; Rinehart, 1969), on the characterization of  
23 the seismic signals recorded around the vent (Kedar et al., 1996, 1998; Kieffer, 1984) or on  
24 the working-out of a dynamic model of the cycle (Hutchinson et al., 1997; Kieffer, 1984).

25 Kieffer (1984) was the first to give an elaborate description of the Old Faithful Geyser  
26 behaviour, including its seismicity and thermodynamics, based on the data collected by  
27 Birch and Kennedy in 1948. She established a model of the rise of water in the conduit  
28 before an eruption (Figure 1) and considered that the collapse of steam bubbles which  
29 cool in the upper part of the water column, is a major physical process that transfers  
30 latent heat to the water column, and produces impulsive acoustic events, which com-  
31 posed the seismic signal recorded at the surface. Hutchinson et al. (1997), using pressure  
32 probes and a small video camera lowered in the conduit, were able to observe different  
33 hydrodynamic processes occurring in the conduit, such as boiling, cavitation, but also  
34 superheated steam expansion, and exsolution of incondensable gas that they proposed  
35 to be  $\text{CO}_2$ . From 1991 to 1994, Kedar and colleagues conducted several seismic surveys  
36 at the surface simultaneously with pressure and temperature measurements in the OFG  
37 conduit (Kedar et al., 1996). During their experiment, an array of 96 short period vertical  
38 geophones, and several broadband sensors were placed around the geyser vent. At the  
39 surface they recorded a quasi harmonic seismic signal composed of the succession of very  
40 impulsive events. They observed that the tremor intensity is modulated by the varia-  
41 tions in the conduit shape during water rise (Kedar et al., 1998). The impulsive events  
42 composing the signal recorded at the surface reverberate in a soft shallow layer and are  
43 not generated by resonance in the water column, as assumed by Kieffer (1984). Finally,  
44 pressure measurements in the conduit confirmed that the individual seismic pulses are  
45 generated by the collapse of bubbles.

46 The goal of this paper is to revisit the data recorded at OFG by Kedar and his  
47 colleagues with the dense array of geophones in order to check how acoustic source lo-  
48 calization techniques derived from ocean acoustics, namely Matched Field Processing  
49 (MFP), can be used to localize the cavitation events recognized by Kieffer and Kedar in  
50 the conduit during the cycle.

51 MFP is a well-established passive technique used to track submarines or marine mam-

52 mals in the ocean, to differentiate animals or to understand their behaviour (Thode et al.,  
53 2000). MFP was recently tested with success on a seismic array of ten sensors deployed on  
54 hydrothermal systems, exhibiting the dominant acoustic source below the array (Legaz  
55 et al., 2009; Vandemeulebrouck et al., 2010). In the present case, the seismic array is  
56 six times denser than during the aforementioned experiments on hydrothermal systems.  
57 Moreover, the seismic sources are shallow and can be associated with in-situ measurements  
58 that provide additional constrains to this study.

### 59 **3 Data**

60 The network deployed by Kedar consists of 96 vertical 1 Hz geophones spread on a tight  
61 grid around the vent of the geyser (Figure 2). The 96 geophones originally recorded  
62 signal during several eruptions with a sampling frequency of 250 Hz, but only 10 minutes  
63 of signal were readily available to be processed in this study. Nevertheless, this 10-minute  
64 interval is associated with a stable stage of the geyser cycle, when the water level is slowly  
65 rising in the conduit approximately 20 minutes before the eruption (Kedar et al. (1998),  
66 see Figure 1). From the array data, a map of the seismic intensity radiated at the surface  
67 around the geyser was calculated at different periods during the cycle by Sharon Kedar  
68 (1996), and the results showed no significant behaviour. Several hammer shots were also  
69 performed to complete the study, in order to look at the difference between the excitation  
70 of the medium by the hammer shot and by the seismic natural impulsive sources.

71 Finally, the analysis of single seismic events recorded on the geophones with a simul-  
72 taneous measurement of the water pressure in the water column at different depths was  
73 performed by Sharon Kedar (Kedar, 1996; Kedar et al., 1996, 1998). The fact that the  
74 record of a pressure pulse near the top surface is followed by the record of an impul-  
75 sive event on the geophones clearly indicates that these events are generated by bubble  
76 collapses in the water column.

77 Thus, the seismic signal recorded in this study is mainly composed of impulsive events  
78 (Figures 3 a and c), with a duration in the order of 0.2 s and with an approximate rate of  
79 100 events per minute (Figure 3 c). During an eruption, it was observed that the number  
80 of events before an eruption follows an asymptotical law (Kedar, 1996), corresponding to  
81 the rise of the water level in the conduit. The 10-min-long record processed in this study  
82 is mainly stable in amplitude and does not show evidence of an eruption (Figure 3 a). It  
83 actually corresponds to a period of approximately 20 minutes before an eruption. The  
84 frequency content of the signal is large with two modes, the first one, the most energetic,  
85 between 10 and 40 Hz and the second one, between 50 and 65 Hz (Figure 3 b).

## 86 **4 Method**

### 87 **4.1 Presentation of the MFP techniques**

88 In volcano seismology, source localization is generally performed on a series of single events  
89 of the same type (Very Long Period, Long Period, Volcano-Tectonic, Tremor). Histor-  
90 ically, time-picking of arrival time has been performed on impulsive volcano-tectonics  
91 events. When this method cannot be used, several other methods exist to localize seismic

92 events recorded on volcanoes. Among these methods, cross-correlation technique permits  
93 to determine the time delays between pairs of station and to compare these delays with  
94 theoretical ones associated to a point source. This technique was applied to localize Long  
95 Period events on Mt Etna (De Barros et al., 2009). The source positions retrieved were  
96 in agreement with the localization given by time-reversal on these same events (O'Brien  
97 et al., 2011). The estimation of the slowness vector has also been applied on volcanic  
98 signals of different types in order to locate their origin (Almendros et al., 2001; Méta-  
99 et al., 2002) as well as on the subduction zone in the Cascades (La Rocca et al., 2010) to  
100 retrieve the location of the tremor sources.

101 Similarly, one can retrieve the source location by looking at the spatial amplitude dis-  
102 tribution for several types of events recorded across a network and comparing it with the-  
103 oretical amplitude decay calculated for a given point source location. Assuming the type  
104 of waves considered, i.e. body waves or surface waves, we can retrieve the source location  
105 which best fits the data (Aki & Ferrazzini, 2000; Battaglia & Aki, 2003). The method was  
106 successfully applied on rockfalls but faced difficulties when considering Volcano-Tectonic  
107 events occurring below the summit of the volcano and below the sea level due to the  
108 complexity of the amplitude distribution in this region.

109 Another technique using a set of similar earthquakes or Long Period events, called mul-  
110 tiplets, consists in determining the difference in origin times between each pair of events  
111 in the multiplet. Localization is then performed by minimizing the residuals between  
112 the time delays between two events and theoretical time delays computed after relative  
113 relocation (Battaglia et al., 2003; Got et al., 1994). Finally, the semblance method was  
114 used on tremors generated by a volcanic eruption in order to follow the migration of the  
115 seismic activity between two potential sources on Izu-Oshima Island volcano in Japan  
116 (Furumoto et al., 1990).

117 In geothermal areas, the seismic signal recorded at the surface of the hydrothermal  
118 system is composed of randomly distributed impulsive events related to bubble collapse  
119 (Ichihara & Nishimura, 2011; Kedar et al., 1998; Legaz et al., 2009; Vandemeulebrouck  
120 et al., 2010). In the case of the present data, the impulsive events often overlap and present  
121 very different signal-to-noise ratio on the geophone array at the surface. This makes time  
122 picking algorithms unefficient to identify and relocalize each event. Furthermore, the  
123 high rate of events ( 100 per minute, see Figure 3 c) would make an event-by-event  
124 relocalization very time consuming. In this perspective, the advantage of the Matched  
125 Field Processing (MFP) technique is to build up a probability of presence of the dominant  
126 acoustic source on a selected time window of the recorded signals. As a matter of fact,  
127 the goal of MFP is to stack the events on a time interval  $T$  in order to provide a robust  
128 relative phase measurement on the whole array. In other words, under the approximation  
129 that most of the bubble collapses in the time window  $T$  come from the same area (within  
130 the half-wavelength), the MFP capitalizes on the phase coherence of these events recorded  
131 on the array. Thus, MFP cumulates the advantage of (1) a better signal-to-noise ratio  
132 through the stacking of events in the time interval  $T$  and (2) an automatic procedure to  
133 localize the dominant seismic source as a function of time for long recordings.

134 Historically, MFP is a localization technique commonly used in ocean acoustics that  
135 starts to be used on hydrothermal systems. This array processing method is a general-  
136 ization of beamforming techniques in the sense that it basically compares phase delays of  
137 forward modeling solutions of the wave equation to acquired data. More precisely, MFP

138 consists in placing a test source at each point of a 3-D search grid, computing the acoustic  
 139 field at all elements of the array and then matching this modelled field with the data.  
 140 The match is maximum when a point source of the search grid is co-located with the true  
 141 point source. The result of the processing is a probability map of the source position.

142 There exist different ways to match the modelled field to the data. The linear method,  
 143 called Bartlett MFP, performs a correlation between the data and the model. The non-  
 144 linear method, in our case the Minimum-Variance Distorsionless Response (MVDR), com-  
 145 putes a maximum-likelihood type minimization between the data and the model. Com-  
 146 pared to Bartlett, the MVDR technique improves the resolution of the MFP output but it  
 147 requires both a good signal-to-noise ratio on the recorded data and a propagation model  
 148 that perfectly adjusts to the data (Jensen et al., 1995). On the other hand, the Bartlett  
 149 MFP gives a robust solution, even for low signal-to-noise ratio, with a spatial resolution  
 150 that is limited to the acoustic wavelength according to diffraction laws.

151 For both linear and non-linear MFP algorithms, the processing is performed in the  
 152 frequency domain as follows.

First, the cross-spectral density matrix (CSDM)  $K$  is calculated as:

$$K = d \cdot d^* \quad (1)$$

153 with  $d = [d_f^1, d_f^2, \dots, d_f^N]$  defined as the acoustic signal at frequency  $f$  recorded on a geo-  
 154 phone  $i$  ( $i$  varying from 1 to  $N$  geophones). The star indicates the complex conjugate  
 155 transpose operation.

Second, a model-based replica vector  $d_m(f, a_i)$  is defined at frequency  $f$  as the mod-  
 elled field from a candidate source position to the array elements, with  $a_i$  being the vector  
 corresponding to the absolute distance between the source candidate position and geo-  
 phone  $i$  of the array. In our case, the propagation model corresponds to the free-space  
 medium which means that the replica vector is expressed by:

$$d_m(f, a_i) = \frac{1}{4\pi a_i} \exp\left(\frac{-2\pi i f a_i}{c}\right). \quad (2)$$

156 In Eq. 2, the free-space monopolar Green's function is chosen as the replica vector since  
 157 we expect to retrieve a local source for which the geophone array is located at one or two  
 158 wavelengths away from the source. In this case, the separation between Rayleigh waves  
 159 and body waves is not effective and wave propagation can be modelled by a velocity  $c$  that  
 160 depends on the medium physical properties. Because of the simple form of the replica  
 161 vector in Eq. 2, MFP could also be described as spherical beamforming. However, more  
 162 complex Green's function could be used as replica vectors in the case of a forward model  
 163 with layering, for example.

The linear MFP (Bartlett) processor is estimated as follows:

$$B_{Bart}(a_i) = \sum_{j=1}^L |d_m^*(f_j, a_i) \cdot K(f_j) \cdot d_m(f_j, a_i)|. \quad (3)$$

Similarly, the non-linear processor (MVDR) output is formulated as:

$$B_{MV}(a_i) = \sum_{j=1}^L \left| \frac{1}{d_m^*(f_j, a_i) \cdot K^{-1}(f_j) \cdot d_m(f_j, a_i)} \right|. \quad (4)$$

164 As shown in Eqs. 3 and 4 above, the MFP is typically averaged incoherently over a  
 165 set of frequencies  $f_1, f_2, \dots, f_L$  in order to improve the contrast of the MFP output.

166 However, the MFP can be processed coherently by considering the cross-correlation  
 167 field instead of the acoustic noise data to construct the cross-spectral density matrix  $K$ .  
 168 The coherent use of MFP implies a coherent average over a discrete number of frequencies  
 169 in the bandwidth of interest, which requires the source signal to be isolated in the data.  
 170 This is done by cross-correlating the noise signal recorded on each element of the array to  
 171 a reference geophone (Figure 4). The coherent approach can be used in two ways. The  
 172 first considers correlations associated with one reference geophone only, then separately  
 173 calculates the MFP using the correlations with different geophones and averages the  
 174 different MFP outputs. A better approach consists in (1) calculating all correlations  
 175 between the geophones and (2) selecting a set of  $p$  correlations that correspond to an  
 176 homogeneous distribution of station pairs among the network, i.e. the inter-station paths  
 177 cover uniformly the whole area (Figure 8 c).

To consider a coherent MFP processing, the set of correlations are transformed into  
 the frequency domain as data vectors at frequencies  $f_1, f_2, \dots, f_L$ . We then create a  
 “supervector”  $\hat{d}$  :

$$\hat{d} = [d_{f_1}^1, d_{f_1}^2, \dots, d_{f_1}^p, \dots, d_{f_L}^1, \dots, d_{f_L}^p], \quad (5)$$

where  $p$  is the number of correlation functions selected among the geophone array. The  
 CSDM is calculated as before:

$$\hat{K} = \hat{d} \cdot \hat{d}^*. \quad (6)$$

Since the data are now issued from correlations between sensor pairs at different fre-  
 quencies, the replica vectors have to follow the same logic. This means that the replica  
 vector is expressed by:

$$\hat{d}_m(f, a_i, a_{ref}) = \frac{1}{16\pi^2 a_i a_{ref}} \exp\left(\frac{-2\pi i f (a_i - a_{ref})}{c}\right). \quad (7)$$

178 where  $a_i$  and  $a_{ref}$  refer now to the distance between the candidate source position and,  
 179 respectively, the  $i$  th geophone or the reference geophone. The model-based replica is  
 180 then compiled into a “supervector”  $\hat{d}_m$  equivalent to the data “supervector” from which  
 181 the linear and non linear coherent MFP are computed as:

$$B_{Bart}(a_i) = |\hat{d}_m^*(a_i) \cdot \hat{K} \cdot \hat{d}_m(a_i)|; \quad (8)$$

$$B_{MV}(a_i) = \left| \frac{1}{\hat{d}_m^*(a_i) \cdot \hat{K}^{-1} \cdot \hat{d}_m(a_i)} \right|. \quad (9)$$

182 It has been shown that the coherent MFP yields better results than the incoherent  
 183 approach for tracking objects in the ocean (Debever & Kuperman, 2007; Michalopoulou &  
 184 Porter, 1996). The disadvantage of coherent processing is that it requires the manipulation  
 185 of large matrices which may considerably increase the computation time.

186 Moreover, a fundamental requirement for MFP processing is that the signal recorded  
 187 at the sensors is coherent from one geophone to another. This often limits its application  
 188 to low frequency as will be shown in the next section. A good first guess is required of the  
 189 medium velocity, especially for the MVDR where small speed mismatch can degrade the  
 190 resolution of the source localization. Two standards are used to evaluate the MFP result:

191 (1) focalization (size of the focal spot) and (2) contrast (ratio between the maximum of  
192 the MFP output and eventual sidelobes).

## 193 4.2 Processing

194 The first step in the MFP processing is the selection of the appropriate frequency band-  
195 width. A few points have to be taken into considerations. First, the higher the frequency,  
196 the shorter the wavelength and the better the spatial resolution of the MFP localization.  
197 MFP is based on the spatial coherence of the recorded signals, which tends to decrease at  
198 higher frequencies and limits the use of large arrays. Furthermore, MFP always applies a  
199 comparison between the data and a wave propagation model. The higher the frequency,  
200 the more complicated the model must be since short wavelengths are typically more sen-  
201 sitive to spatial heterogeneities. Finally, the propagation model used for MFP in the case  
202 of a broad frequency bandwidth must also include a frequency-dependent velocity profile.  
203 A balance between MFP resolution at high frequencies and robust MFP localization at  
204 low frequencies is problem-specific and must be determined on a case by case basis.

205 In the case of Old Faithful data, the spatial coherence was first calculated from 8 to 70  
206 Hz. The coherency is high between 12 and 58 Hz, while the signals are most energetic in  
207 the frequency band 10 to 40 Hz (Figure 3 b). Finally, comparing the MFP results in the  
208 5-15 Hz and 20-30 Hz bands, it appeared that the focalization and the contrast are better  
209 in the lower frequency band. The MFP was then processed between 5 Hz and 15 Hz with  
210 a 1 Hz sliding frequency window, and the contrast and the focalization were optimal at  
211 12 Hz.

212 In the second step, an estimation of the seismic velocity was performed using the  
213 records of 12 hammer shots made by Sharon Kedar in 1992. This analysis revealed that  
214 the mean surface velocity is  $\sim 130 \text{ ms}^{-1}$  between 11 and 13 Hz, with a low-velocity area  
215 in the South part of the network. This zone of lower velocity could be associated with  
216 softer sediments deposited in a small stream area. When performing MFP, we have used  
217 this mean surface velocity ( $130 \text{ ms}^{-1}$ ) in a 1-D tabular model. The vertical gradient was  
218 estimated from a velocity model of S. Kedar (1996) using shear waves velocity model, as  
219 shown in Figure 5 and is of  $23.5 \text{ ms}^{-1}/\text{m}$ .

220 In the final step, we selected the sensors to be used with the incoherent processing or  
221 the sensor pairs in the case of coherent processing. Sensors located in a lower velocity  
222 zone and showing a degraded spatial coherence were rejected (Figure 4). For coherent  
223 MFP processing, we restricted our choice to five reference stations among the network  
224 in order to (1) provide homogeneous spatial distribution of the station pairs while (2)  
225 limiting the size of the  $\hat{K}$  and thus the computation time of the MFP processing.

## 226 4.3 Results and discussion

227 The 10 minutes of recorded signal were processed in order to localize and monitor the dom-  
228 inant noise source position. The signals were truncated into chunks of  $T=20\text{s}$  time window  
229 from which coherent/incoherent MFP was performed using either the linear Bartlett or  
230 non-linear MVDR method.

231 Figures 6 and 7 shows incoherent MFP results for one  $T=20\text{s}$  time window using  
232 Bartlett and MVDR processing. The MFP results are displayed as 3-D maps that cor-



233 respond to the probability of presence of the noise source (Figures 6 a and 7 a). We  
234 first notice that both linear/non-linear MFP give the same general source position. The  
235 spatial resolution of the MFP is evaluated from slices in the X-Y, X-Z and Y-Z planes  
236 at the MFP maximum (Figures 6 b-d and 7 b-d). As expected, the incoherent MVDR  
237 performs better than the Bartlett in terms of spatial focalization. Indeed, the spatial res-  
238 olution of the linear Bartlett MFP is limited to the half-wavelength ( $\sim 6.5$  m) according  
239 to diffraction laws while the non-linear MVDR MFP outpasses this limit with a  $\sim 2$  m  
240 spatial resolution.

241 When compared to incoherent MFP, coherent MFP does not improve the focalization  
242 results as shown in Figures 8 a and b. Compared to ocean where coherent processing  
243 significantly improved the focalization performance (Debever & Kuperman, 2007), the  
244 optimal focalization limit was already reached with incoherent MFP in this case thanks  
245 to the high signal-to-noise ratio of the seismic signals and the dense spatial coverage  
246 provided by the geophone array around the geyser vent.

247 To confirm the validity of the MFP results, travel times were calculated between  
248 the MFP source position and each sensor according to the velocity model plotted in  
249 Figure 5. When compared to a reference geophone, these theoretical time-delays were  
250 then superimposed to the cross-correlation function with the same reference geophone  
251 (Figure 4). The satisfactory adjustment of the theoretical time-delays with the dominant  
252 cross-correlation wavefront over most of the geophone array is an a posteriori validation of  
253 MFP results. The discrepancy observed for sensors 17 to 20 may be due to wrong station  
254 coordinates or to the presence of a strong spatial heterogeneity in the medium.

255 The 12-m depth of the noise source is consistent with in-situ observations (Hutchinson  
256 et al., 1997). The temperature measurements made by Birch & Kennedy (1972) indicate  
257 a stationarity of the water level in the conduit during the same cycle period, which was  
258 confirmed by Hutchinson et al. (1997). Furthermore, in-situ observations with a camera  
259 made by Hutchinson revealed the presence of a widening of the conduit between 10.5  
260 and 14 m. The horizontal location of the source with the different MFP processors  
261 closely corresponds to the orifice position (Figures 8 a and b). The digression of the  
262 source position from the horizontal location of the vent maybe due to the widening of the  
263 conduit at depth. This shift could also be attributed to the uncertainty on the velocity  
264 model and the geophone positions.

265 The monitoring of the noise source inside the vent was performed for each successive  
266  $T=20$ s time-window with an overlap of 75%. The spatial localization of the noise sources  
267 is shown in Figures 9 a-c, showing stable results during the 10-min-long recording. The  
268 standard deviation of the source position in the X and Y direction is 0.30 m, while standard  
269 deviation is slightly larger in the Z direction with a value of 0.42 m. More precisely, the  
270 source depth shows periodic variation with a dominant period slightly less than 1 minute  
271 (Figures 9 d and e). This period may be associated with temperature oscillation observed  
272 at this depth (Hutchinson et al., 1997), likely due to two-phase flow static instabilities  
273 (Bouré et al., 1973).

## 274 5 Conclusion

275 The efficiency of the MFP method was demonstrated in retrieving the location of the  
276 dominant noise source in hydrothermal systems.

277 Using a velocity model (Kedar, 1996) and the mean surface velocity calculated using  
278 hammer shots, the origin of the seismic signals recorded at Old Faithful Geyser on a  
279 geophone network at the surface is in good agreement with in-situ measurements. The  
280 dominant seismic source location during this period of record corresponds to a steady  
281 state with continuous boiling rate at a given constant depth ( $\sim 12$  m).

282 The data processing using different MFP techniques show similar source locations.  
283 Differences in the MFP results concern the spatial width of the focalization according to  
284 the MFP technique. The MVDR MFP proved to provide higher resolution results than  
285 the Bartlett MFP for all cases analyzed in this study, resulting in a  $\sim 2$  m source resolution  
286 for the MVDR MFP, compared to  $\sim 4$  m resolution for Bartlett MFP.

287 The time-evolution of the source location of the multiple impulsive events was continu-  
288 ously followed during a 10-min-long steady period of seismic activity and showed a stable  
289 source position, with fluctuations of small amplitude (less than 50 cm) and a period less  
290 than one minute. Applying MFP techniques on longer data set, comprising several cycles,  
291 would permit to perform a temporal monitoring of the acoustic source and to improve  
292 the understanding of the geyser dynamics.

293 Furthermore, the MFP method could be an interesting tool to monitor other volcanic  
294 signals like volcano-tectonic event (VT) or long period event (LP).

## 6 acknowledgments

Most of the computations presented on this article were performed at the Service Commun de Calcul Intensif de l'Observatoire de Grenoble (SCCI). The Digital Elevation Model used in this study is based on data services provided by the OpenTopography Facility with support from the National Science Foundation under NSF Award Numbers 0930731 and 0930643 and is based on services provided by the Plate Boundary Observatory operated by UNAVCO for EarthScope (<http://www.earthscope.org>) and supported by the National Science Foundation (No. EAR-0350028 and EAR-0732947). We would like to thank Shaul Hurwitz and Robert Clayton for their help.

## References

- Aki, K. & Ferrazzini, V., 2000. Seismic monitoring and modeling of an active volcano for prediction, *J. geophys. Res.*, **105**(B7), 16,617–16,640.
- Almendros, J., Chouet, B., & Dawson, P., 2001. Spatial extent of a hydrothermal system at Kilauea Volcano, Hawaii, determined from array analyses of shallow long-period seismicity. 1. Method, *J. geophys. Res.*, **106**(B7), 13565–13580.
- Battaglia, J. & Aki, K., 2003. Location of seismic events and eruptive fissures on the Piton de la Fournaise Volcano using seismic amplitudes, *J. geophys. Res.*, **108**(B8), 2364.
- Battaglia, J., Got, J.-L., & Okubo, P., 2003. Location of long-period events below Kilauea Volcano using seismic amplitudes and accurate relative relocation, *J. geophys. Res.*, **108**(B12), 2553.
- Birch, F. & Kennedy, G. C., 1972. Notes on geyser temperatures in Iceland and Yellowstone National Park, *Flow and fracture of rocks: American Geophysical Union Geophysical Monograph*, **16**, 329–336.
- Bouré, J., Bergles, A., & Tong, L., 1973. Review of two-phase flow instability, *Nuclear Engineering and Design*, **25**(2), 165–192.
- De Barros, L., Bean, C. J., Lokmer, I., Saccorotti, G., Zuccarello, L., O’Brien, G. S., Métaxian, J.-P., & Patané, D., 2009. Source geometry from exceptionally high resolution long period event observations at Mt Etna during the 2008 eruption, *Geophys. Res. Lett.*, **36**(24), L24305.
- Debever, C. & Kuperman, W. A., 2007. Robust matched-field processing using a coherent broadband white noise constraint processor, *J. acoust. Soc. Am.*, **122**(4), 1979–1986.
- Fournier, R. O., 1989. Geochemistry and dynamics of the Yellowstone National Park hydrothermal system, *Annu. Rev. Earth planet. Sci.*, **17**(1), 13–53.
- Furumoto, M., Kunitomo, T., Inoue, H., Yamada, I., Yamaoka, K., Ikami, A., & Fukao, Y., 1990. Twin sources of high-frequency volcanic tremor of Izu-Oshima Volcano, Japan, *Geophys. Res. Lett.*, **17**(1), 25–27.
- Got, J.-L., Fréchet, J., & Klein, F. W., 1994. Deep fault plane geometry inferred from multiplet relative relocation beneath the south flank of Kilauea, *J. geophys. Res.*, **99**(B8), 15375–15386.
- Hurwitz, S., Kumar, A., Taylor, R., & Heasler, H., 2008. Climate-induced variations of geyser periodicity in Yellowstone National Park, USA, *Geology*, **36**(6), 451–454.
- Husen, S., Smith, R. B., & Waite, G. P., 2004. Evidence for gas and magmatic sources beneath the Yellowstone volcanic field from seismic tomographic imaging, *J. Volc. Geotherm. Res.*, **131**(3-4), 397–410.

- Hutchinson, R. A., Westphal, J. A., & Kieffer, S. W., 1997. In situ observations of Old Faithful Geyser, *Geology*, **25**(10), 875–878.
- Ichihara, M. & Nishimura, T., 2011. Pressure impulses generated by bubbles interacting with ambient perturbation, *Extreme Environmental Events*, pp. 731–752.
- Jensen, F. B., Kuperman, W. A., Porter, M. B., Schmidt, H., & Bartram, J. F., 1995. *Computational Ocean Acoustics*, American Institute of Physics, New York, (578 pp.).
- Kedar, S., 1996. *The origin of harmonic tremor at Old Faithful*, Ph.D. thesis, Caltech.
- Kedar, S., Sturtevant, B., & Kanamori, H., 1996. The origin of harmonic tremor at Old Faithful Geyser, *Nature*, **379**, 708–711.
- Kedar, S., Kanamori, H., & Sturtevant, B., 1998. Bubble collapse as the source of tremor at Old Faithful Geyser, *J. geophys. Res.*, **103**, 24,283–24,299.
- Kieffer, S. W., 1984. Seismicity at Old Faithful Geyser: an isolated source of geothermal noise and possible analogue of volcanic seismicity, *J. Volc. Geotherm. Res.*, **22**(1-2), 59-95.
- La Rocca, M., Galluzzo, D., Malone, S., McCausland, W., & Del Pezzo, E., 2010. Array analysis and precise source location of deep tremor in Cascadia, *J. geophys. Res.*, **115**, B00A20.
- Legaz, A., Revil, A., Roux, P., Vandemeulebrouck, J., Gouédard, P., Hurst, T., & Bolève, A., 2009. Self-potential and passive seismic monitoring of hydrothermal activity: A case study at Iodine Pool, Waimangu geothermal valley, New Zealand, *J. Volc. Geotherm. Res.*, **179**(1-2), 11 – 18.
- Métaxian, J.-P., Lesage, P., & Valette, B., 2002. Locating sources of volcanic tremor and emergent events by seismic triangulation: Application to Arenal volcano, Costa Rica, *J. geophys. Res.*, **107**(B10), 2243.
- Michalopoulou, Z.-H. & Porter, M. B., 1996. Matched-field processing for broad-band source localization, *IEEE Journal of Oceanic Engineering*, **21**, 384–392.
- Miller, D. S. & Smith, R. B., 1999. P and S velocity structure of the Yellowstone volcanic field from local earthquake and controlled-source tomography, *J. geophys. Res.*, **104**(B7), 15105–15121.
- O’Brien, G. S., Lokmer, I., De Barros, L., Bean, C. J., Saccorotti, G., Métaxian, J.-P., & Patané, D., 2011. Time reverse location of seismic long-period events recorded on Mt Etna, *Geophys. J. Int.*, **184**(1), 452–462.
- Rinehart, J., 1969. Old Faithful Geyser performance 1870 through 1966, *Bull. Volcanol.*, **33**(1), 153–163.
- Thode, A. M., D’Spain, G. L., & Kuperman, W. A., 2000. Matched-field processing, geoacoustic inversion, and source signature recovery of blue whale vocalizations, *J. acoust. Soc. Am.*, **107**(3), 1286–1300.

Vandemeulebrouck, J., Roux, P., Gouédard, P., Legaz, A., Revil, A., Hurst, A., Bolève, A., & Jardani, A., 2010. Application of acoustic noise and self-potential localization techniques to a buried hydrothermal vent (Waimangu Old Geyser site, New Zealand), *Geophys. J. Int.*, **180**(2), 883–890.

Figure 1 : Water level in the conduit of Old Faithful before an eruption reported by Birch & Kennedy (1972), from an adaptation of Kieffer (1984).

Figure 2 : (a) Shaded relief map of Old Faithful area. Coordinates are indicated in [m UTM]. (b) Topographic map and location of the 96 vertical 1 Hz geophones around the vent of Old Faithful Geyser. Elevation contour interval is one meter. The red square corresponds to the grid where the MFP was processed. The reference coordinates of the geyser vent are  $X=513,672.51$  m UTM,  $Y=4,923,032.42$  m UTM and  $Z=2240$  m.

Figure 3 : A 10-minute-long record at geophone 90. a): 10 minutes record. b): Average amplitude spectrum calculated over the 96 geophones. c): Zoom between 300 and 310 s.

Figure 4 : Cross-correlation of 10 minutes of seismic signal recorded on the 96 geophones with the sensor 54 as reference. The signals are bandpass filtered between 10 and 14Hz. The symbols correspond to theoretical delays associated with the point source retrieved with MFP ( $X=-1.35$  m,  $Y=1.65$  m and  $Z=11$  m) in a 1-D model with a vertical gradient of velocity of  $23.5 \text{ ms}^{-1}/\text{m}$  and a surface velocity of  $130 \text{ ms}^{-1}$ , the black stars indicate the sensors used for the processing and the magenta circles are associated to sensors that were disregarded in the MFP processing.

Figure 5 : A velocity model proposed by Kedar (1996) compared to the velocity model used for the localization.

Figure 6 : (a) 3-D Incoherent Bartlett output between 11.5 and 12.5 Hz for a medium with a velocity of  $130 \text{ ms}^{-1}$  at surface and a gradient of velocity of  $23.5 \text{ ms}^{-1}/\text{m}$ , with (b) slice in the plane X-Z, (c) slice in the plane Y-Z and (d) slice in the plane X-Y. The white circle corresponds to the horizontal vent location. The source was determined using the search grid represented on Figure 2 (b).

Figure 7 : (a) 3-D Incoherent MVDR output between 11.5 and 12.5 Hz for a medium with a velocity of  $130 \text{ ms}^{-1}$  at surface and a gradient of velocity of  $23.5 \text{ ms}^{-1}/\text{m}$ , with (b) slice in the plane X-Z, (c) slice in the plane Y-Z and (d) slice in the plane X-Y. The white circle corresponds to the horizontal vent location. The source was determined using the search grid represented in red on Figure 2 (b).

Figure 8 : Estimated locations of the seismic sources using the whole 10 minutes of signal according to the MFP method. Each error bar refers to the spot width measured at 70% of the maximum. The methods used are B: Bartlett and M: MVDR. These methods were processed (a): incoherently, (b): coherently with correlations calculated between 11.5 and 12.5 Hz from  $p=171$  station pairs. The dotted lines on gray represent the position of the vent at the surface. (c): Number of paths per cell projected on a  $70 \times 70$  m grid with 5-m squared cells around the geyser position for the stations pairs selected for the coherent MFP.

Figure 9 : (a) Location of the seismic sources in a X-Y plane during 10 minutes of signal determined with coherent Bartlett processed on 20-s-long-windows and with an overlap of 75% . The position of the source is relative to the position of the vent. (b) Location of the seismic sources on a X-Z plane and (c) on a Y-Z plane. (d) Location of the seismic source in depth according to the time. (e) Fourier Transform of the source position dynamics averaged on the X, Y and Z directions.

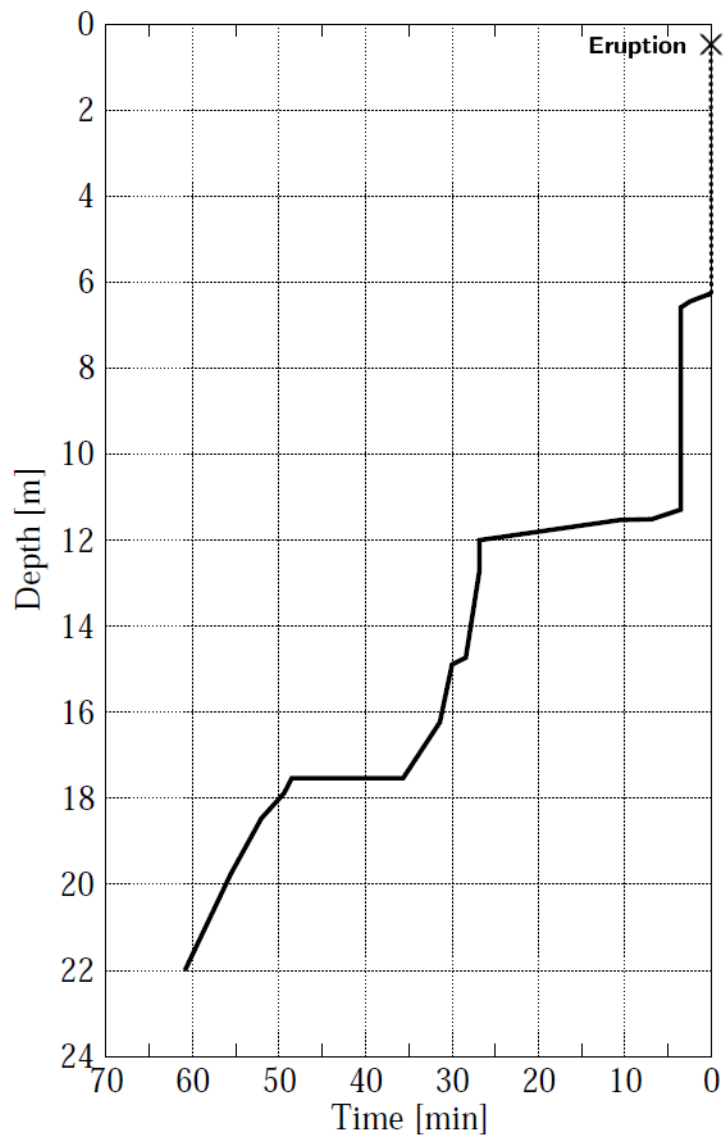


Figure 1



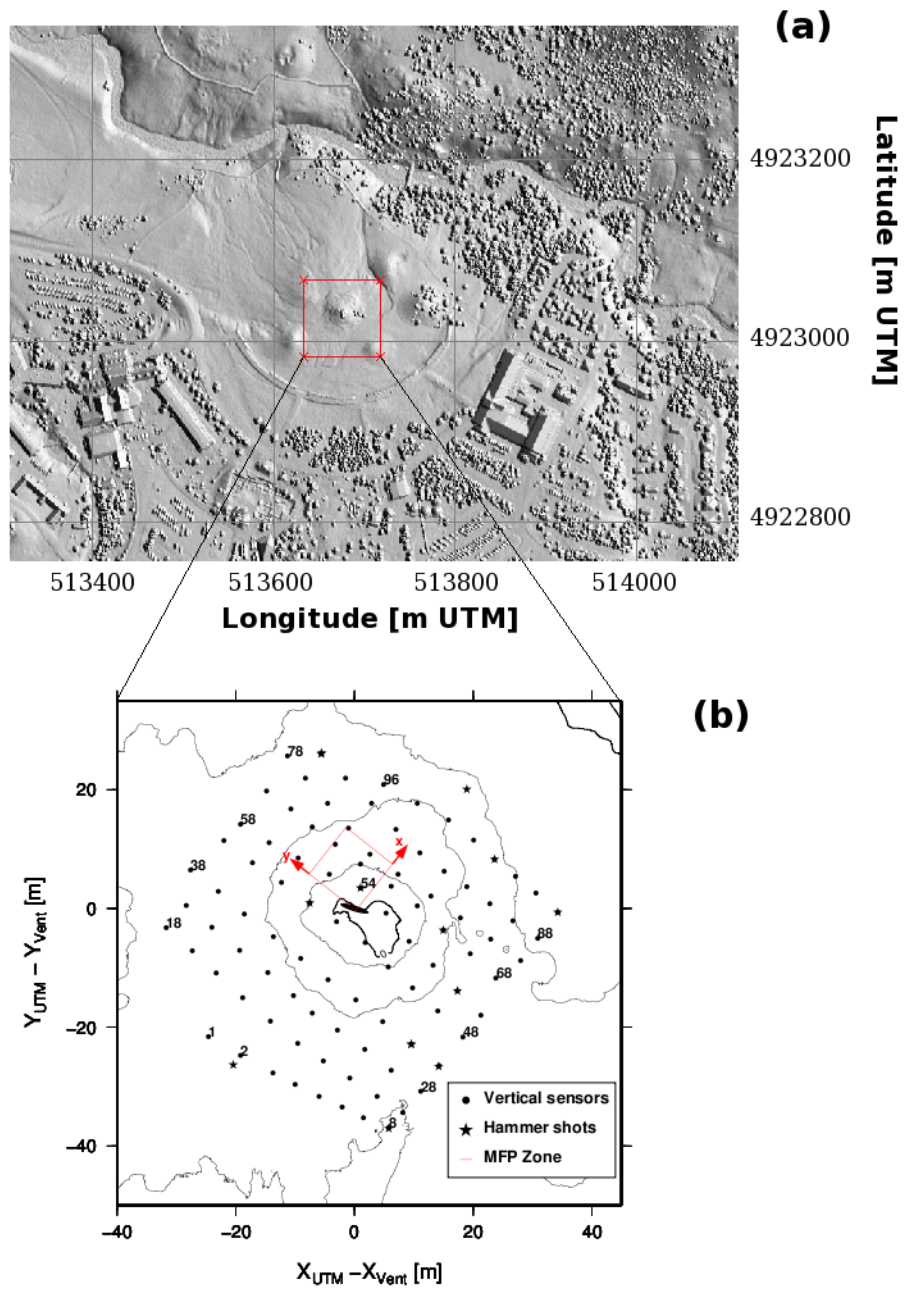


Figure 2

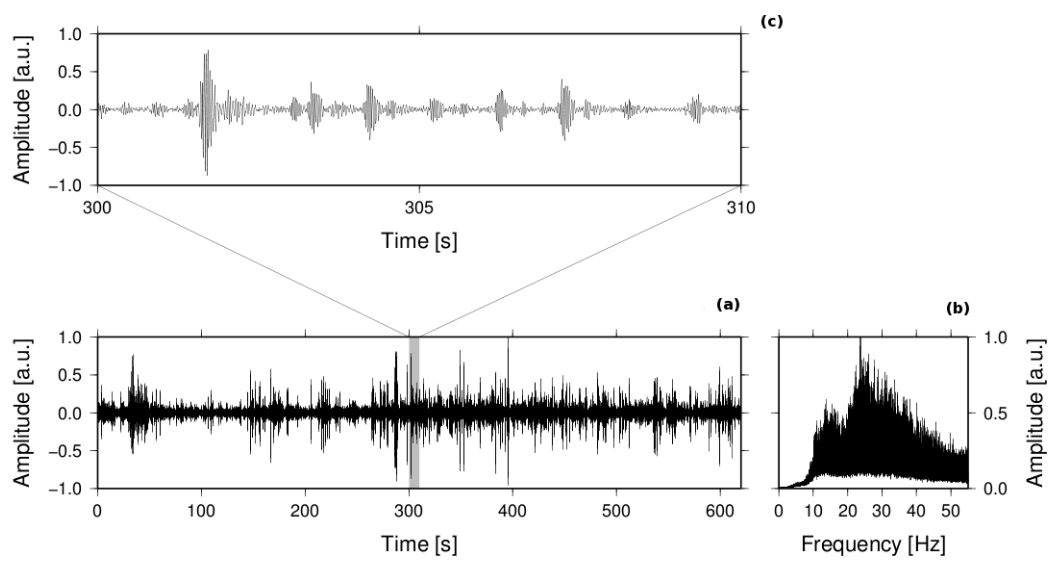


Figure 3

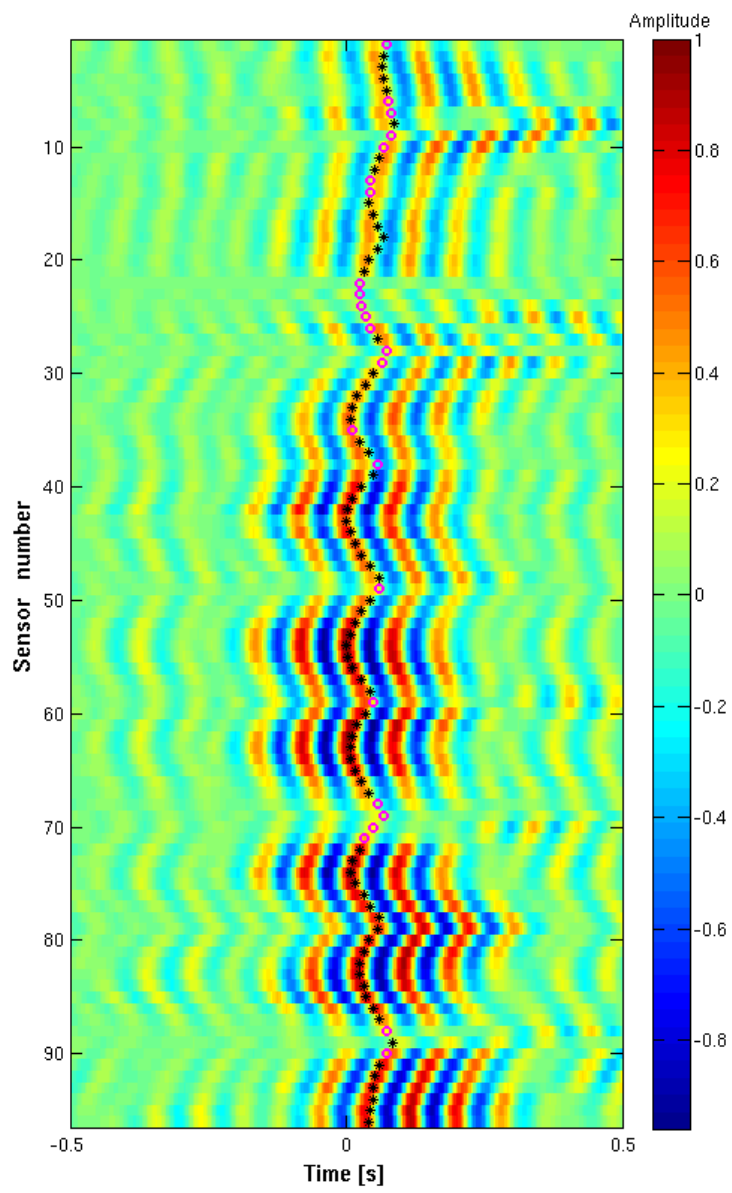


Figure 4

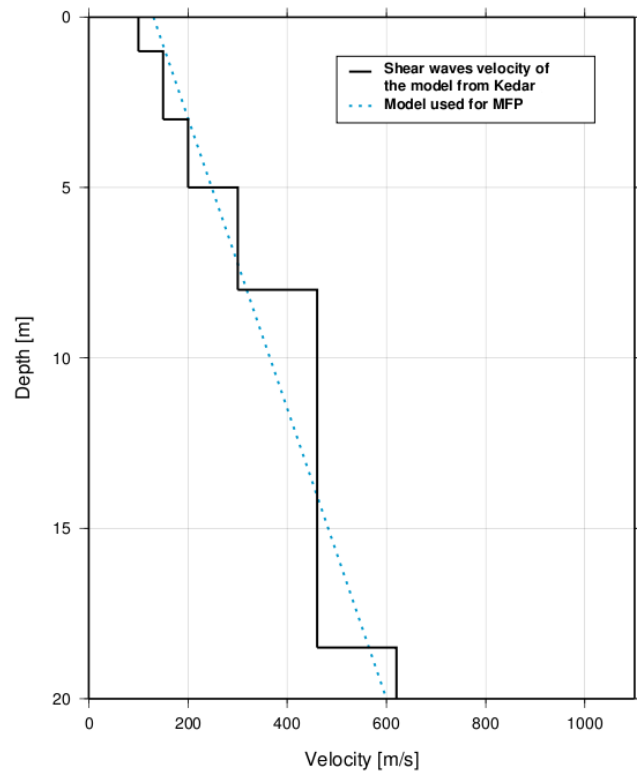


Figure 5

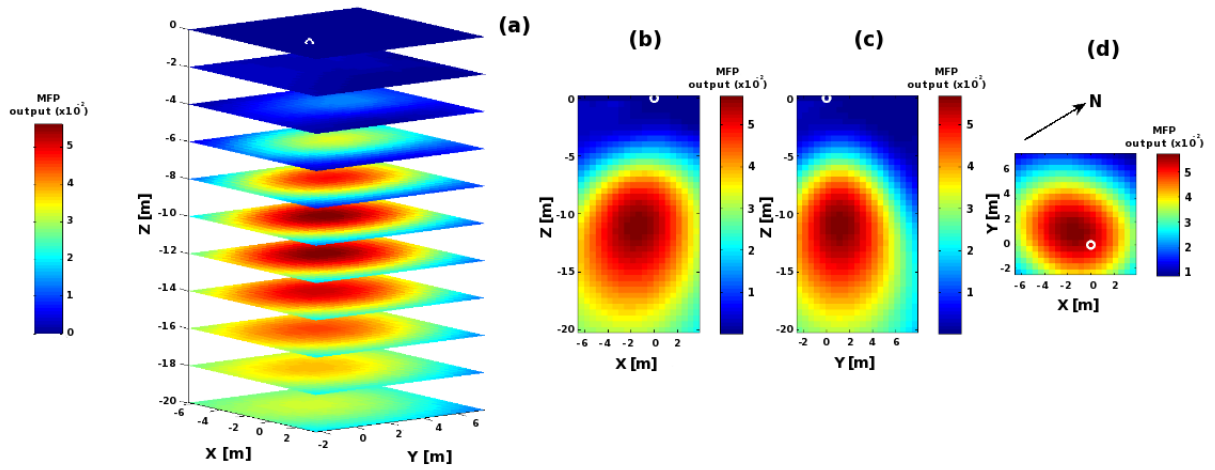


Figure 6

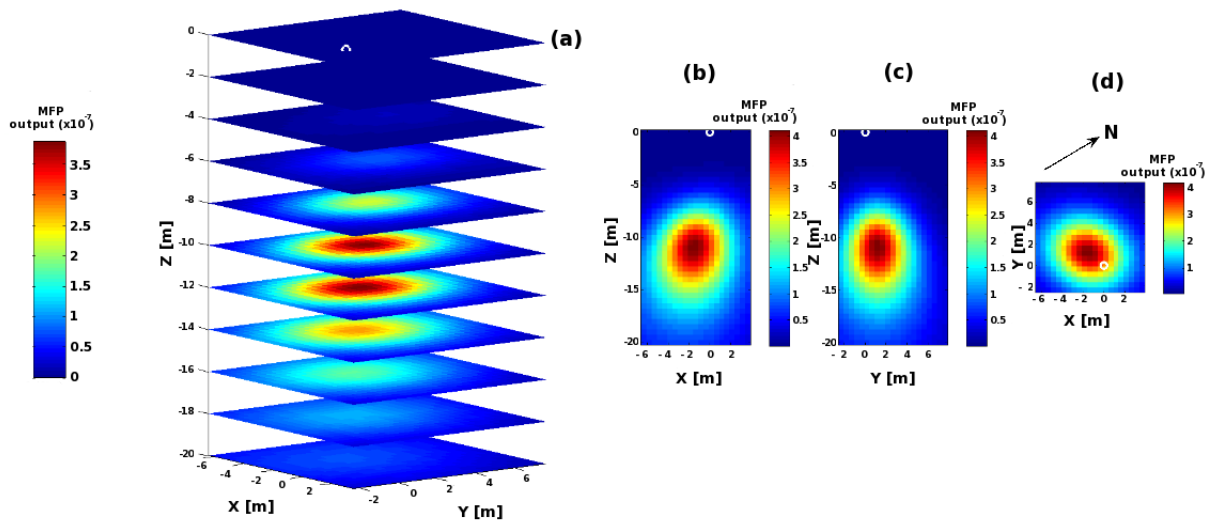


Figure 7

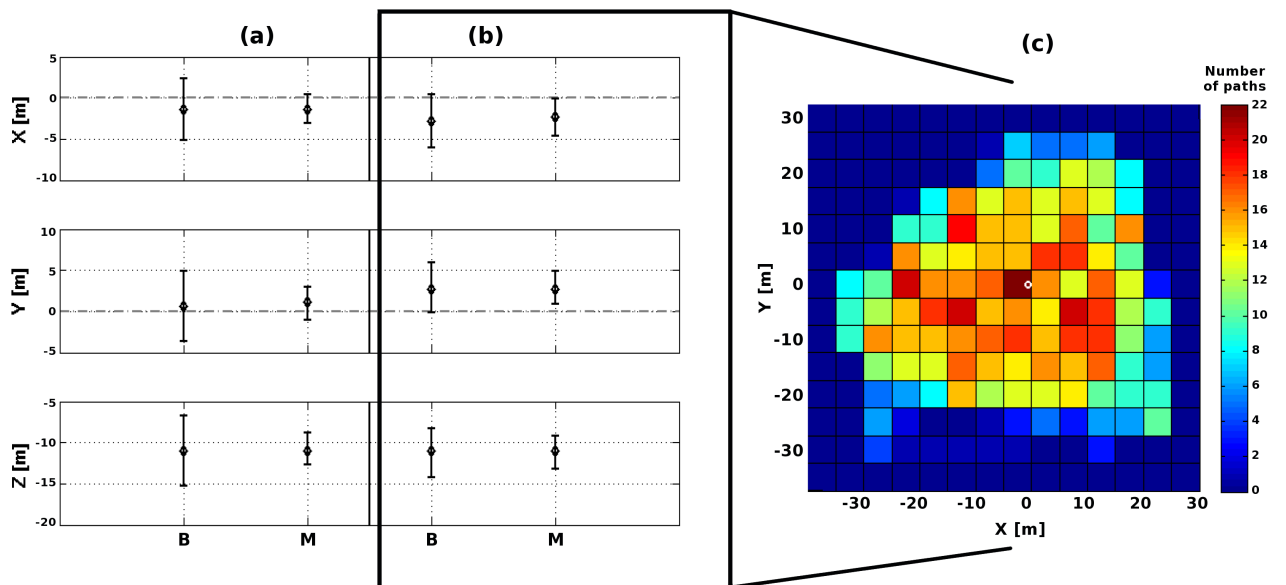


Figure 8

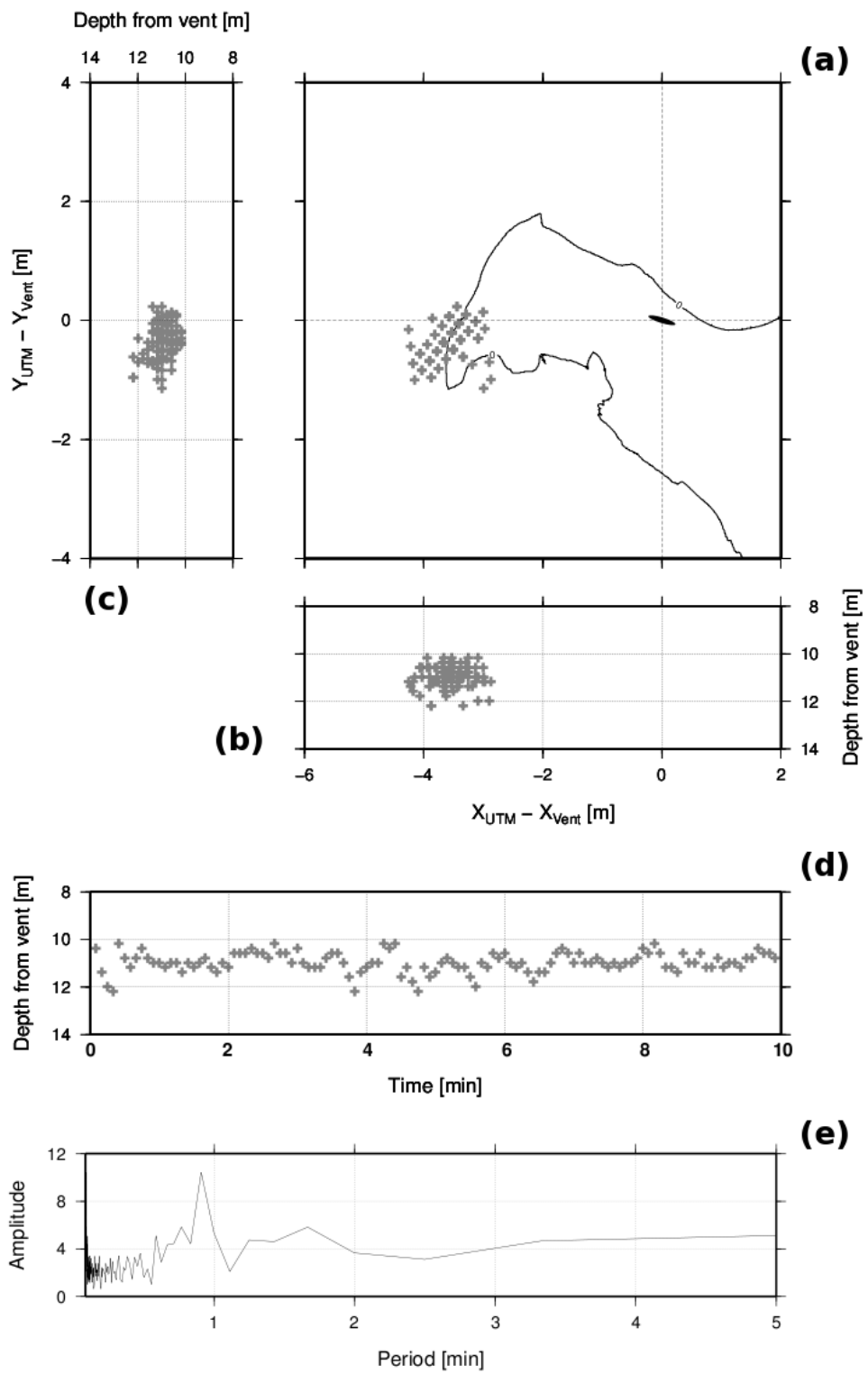


Figure 9